Supplementary Information (SI) for Journal of Materials Chemistry C.
This journal is © The Royal Society of Chemistry 2025

Supporting Information

Synergistic Effects of Pd Single Atoms and Nanoclusters Boosting SnO_2 Gas Sensing Performance

Yaprak Ozbakir [a, b], *Yong Xia* [c, d], *Aifei Pan* [d], *Jiyun Hong* [e], *Jorge E. Perez-Aguilar* [e], *Simon R. Bare* [e], *Francesca Rossi* [f], *Rohan Dhall* [g], *Afnan Ali Alghannam* [a], *Nishit Goel* [h], *Stephen Bart* [h], *Carlo Carraro* [a, b], and *Roya Maboudian* [a, b, *]

[a] Department of Chemical and Biomolecular Engineering, University of California, Berkeley, CA 94720, United States

[b] Berkeley Sensor & Actuator Center, Berkeley, CA 94720, United States

[c] School of Instrument Science and Technology, Xi'an Jiaotong University, Xi'an 710049, China

[d] State Key Laboratory for Manufacturing Systems Engineering, and International Joint Laboratory for Micro/Nano Manufacturing and Measurement Technologies, Xi'an Jiaotong University, Xi'an, 710049, China

[d] State Key Laboratory for Manufacturing Systems Engineering, and International Joint Laboratory for Micro/Nano Manufacturing and Measurement Technologies, Xi'an Jiaotong University, Xi'an, 710049, China

[e] SSRL, SLAC National Accelerator Laboratory, Menlo Park, California 94025, U.S.A.

[f] IMEM-CNR Institute, 43124 Parma, Italy

[g] National Center for Electron Microscopy (NCEM), Lawrence Berkeley National Laboratory, Berkeley, CA 94720, U.S.A.

[h] TDK InvenSense Inc., San Jose, California 95110, U.S.A.

Table of Contents for

* Corresponding author email: maboudia@berkeley.edu

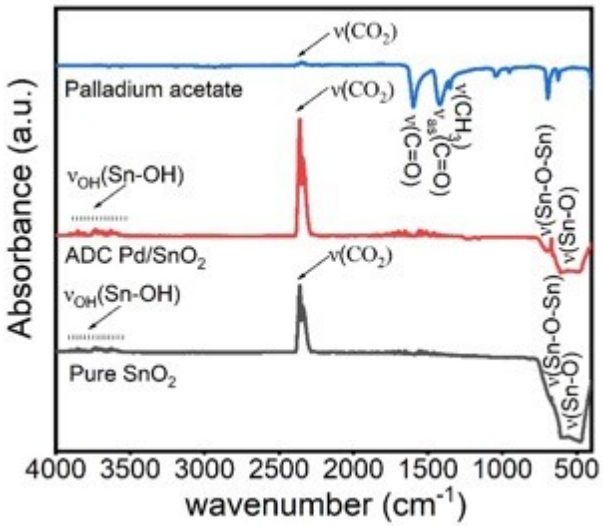

Figure S1. FTIR spectra of palladium acetate, ADC Pd/SnO_2, and pure SnO_2. The band at 2360 cm^{-1} is assigned to atmospheric CO_2.

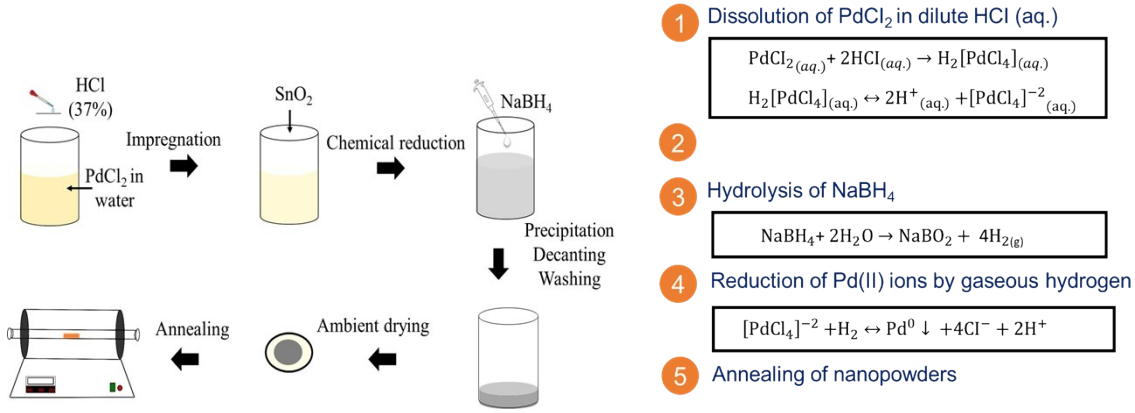

Scheme S1. Preparation of Pd nanoparticles on SnO_2

Preparation of Pd nanoparticles on SnO_2

For comparison, Pd nanoparticles loaded onto SnO_2, labeled as Pd NPs/SnO_2, was synthesized via wet impregnation of Pd precursor onto SnO_2 support and chemical reduction of Pd ions, followed by an annealing step (Scheme S1). $PdCl_2$ was employed as the Pd^{2+} precursor, and sodium borohydride ($NaBH_4$) was used as the reducing agent to reduce the Pd metal ions into Pd metal nanoparticles. 24 mg $PdCl_2$ was dissolved in 100 ml DI water in the presence of a few drops of concentrated hydrochloric acid. and stirred until it was completely dissolved. 0.5 g of SnO_2 was then added in the $PdCl_2$ solution under continuous stirring at room temperature for 3 h. Following the impregnation of Pd complex onto the SnO_2 nanocrystals, 3 ml of 87.2 mM fresh

$NaBH_4$ solution was added into the solution under stirring for 3h to reduce the Pd metal ions. The color of the suspension changed from yellow to gray, which indicates that Pd nanoparticles precipitated on the SnO_2 nanocrystals. The prepared Pd NPs/SnO_2 catalysts were washed with DI water and ethanol several times, respectively, and the precipitate was dried at room temperature overnight. Finally, the obtained gray powder was annealed at 500 °C in atmospheric air at ambient pressure for 3h, which yielded brownish powder. The presence of Pd, Sn and O in the full spectrum scan of XPS in Figure S11 is evidenced without any impurity elements, suggesting complete removal of Cl^- and the formation of Pd-O-Sn based catalyst.

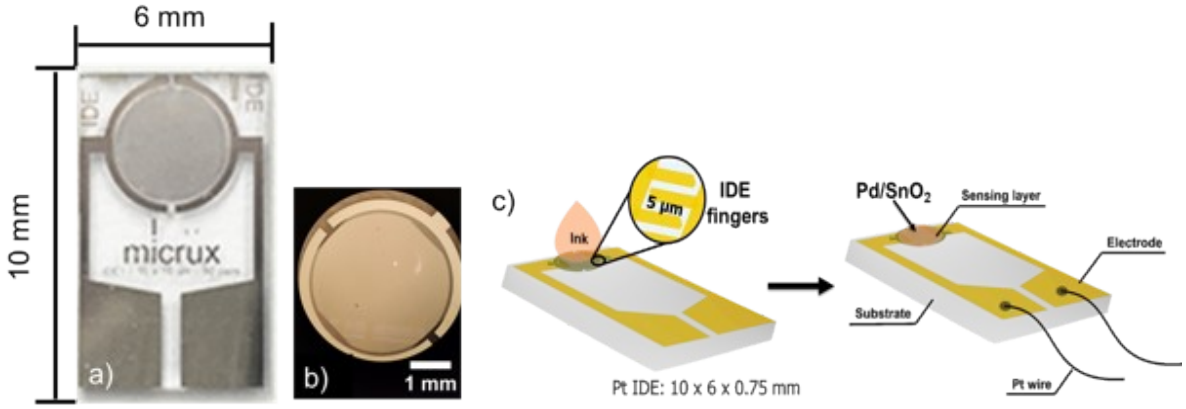

Figure S2. Chemiresistive gas sensor fabrication: a) Optical image of a Pt/Ti IDE with an active area of 3.5 mm in length, composed of 90 finger pairs of 5 µm width and spacing between each parallel electrode finger on glass substrate (10 x 6 x 0.75 mm). b) Optical image of the active area of the Pt/Ti IDE. c) Schematic of senor fabrication following drop-casting a colloidal solution of the as-synthesized catalysts onto the pre-cleaned Pt-Ti interdigitated electrode; evaporation of the solvent; and post-deposition annealing treatment of the deposited sensing layer; and subsequently conductive wire-bonding.

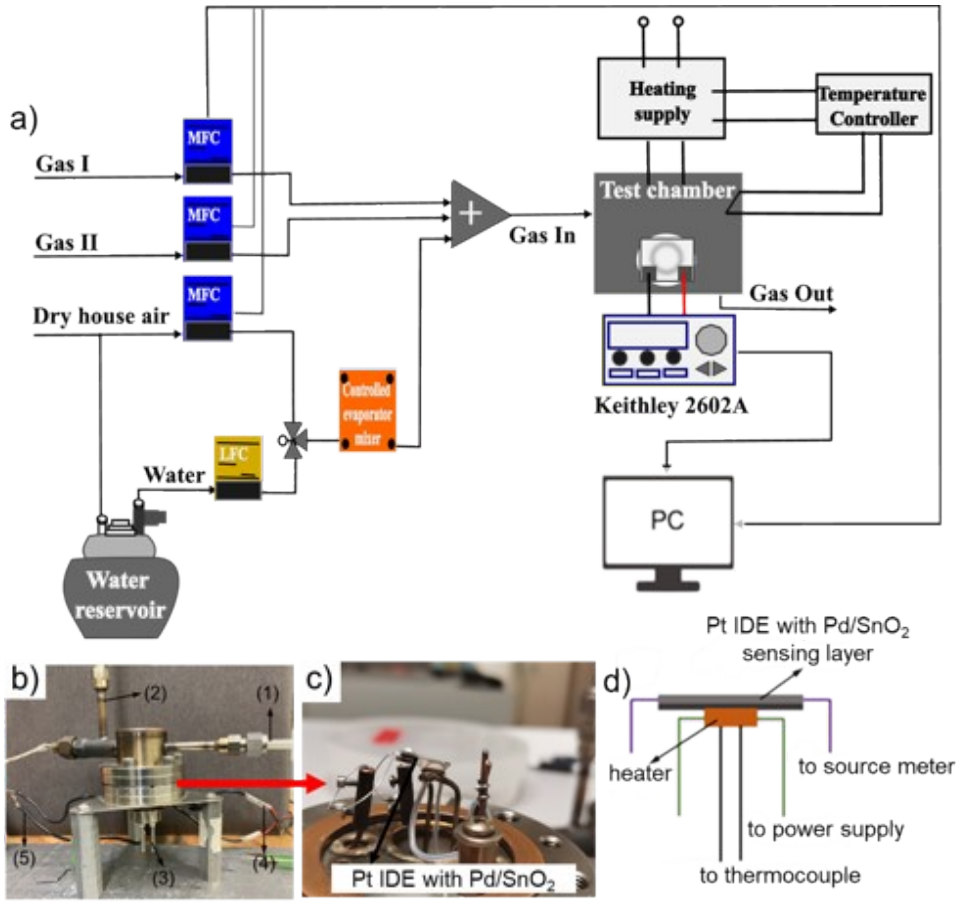

Figure S3. Gas sensing test apparatus: (a) Gas delivery system and gas sensing test setup. (b) Photo of the test chamber: (1) gas inlet; (2) gas outlet; (3) to thermocouple to measure the temperature of the heater; (4) to DC heater power supply to control the operating temperature of the sensor; (5) to source meter to measure the resistance of the sensor. (c) Internal view of the test chamber with Pd/Ti electrode installed. (d) Schematic diagram of the side-view of the sensor, heater, and electrical connections.

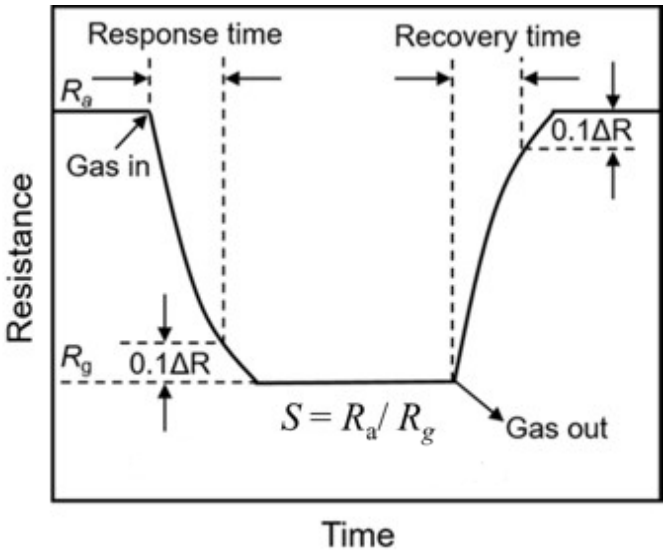

Figure S4. Definition of sensor response, response and recovery times.

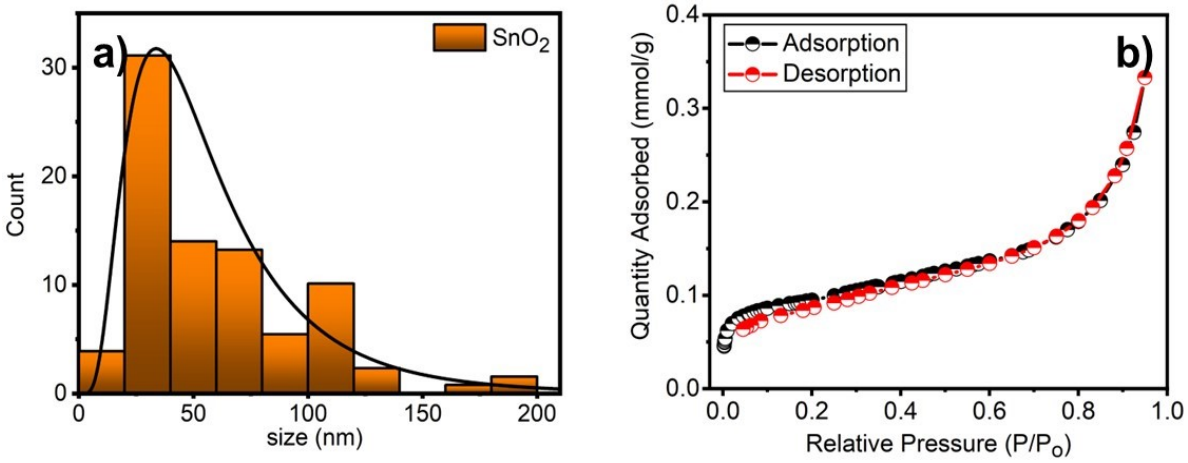

Figure S5. **a)** Particle size distribution histogram for the STEM image of SnO_2 support in Figure 1 in the main text. Scale bar, 50 nm. **b)** Nitrogen adsorption-desorption isotherm of SnO_2 support at 77 K. About 180 mg of SnO_2 support pre-annealed at 500 °C was degassed at 300 °C overnight before analysis. N_2 adsorption-desorption isotherm of annealed SnO_2 suggests type II isotherm, typical for non-porous materials, on which total Brunauer–Emmett–Teller (BET) surface area was calculated as 7.5 $m^2.g^{-1}$.

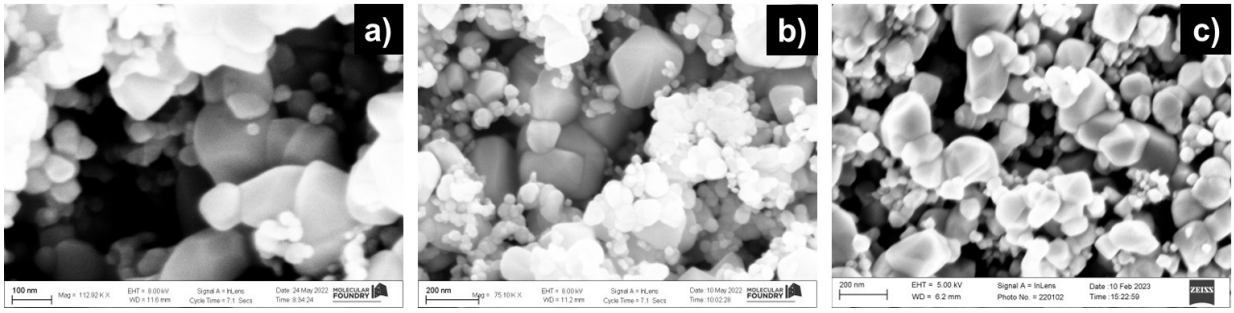

Figure S6. Representative FESEM images of a) SnO_2, b) Pd NPs/SnO_2 and ADC Pd /SnO_2, respectively. Scale bars, 100 nm, 200 nm, respectively.

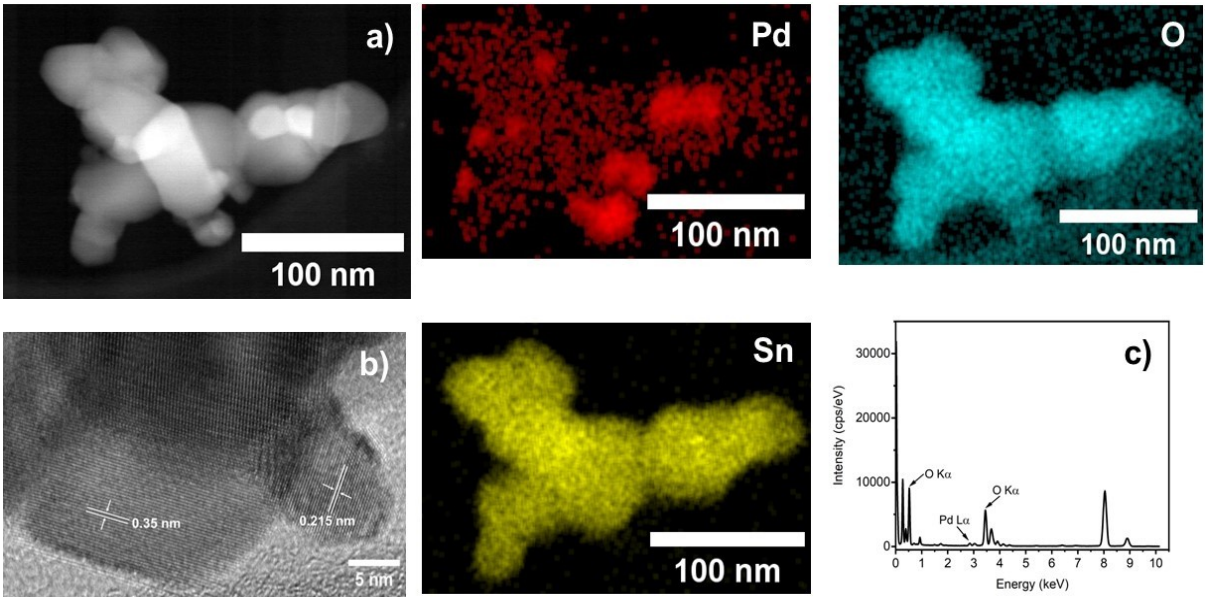

Figure S7. a) STEM image of Pd NPs/SnO_2 and its corresponding EDS elemental mapping images of Pd, O and Sn. Scale bars, 100 nm. b) HRTEM image of Pd NPs/SnO_2. Scale bar, 5 nm. c) EDS analysis showing presence of Pd element in the Pd NPs/SnO_2.

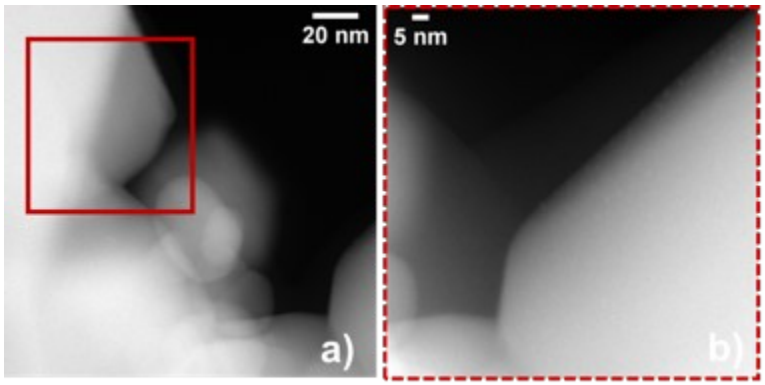

Figure S8. Structural and morphological characterization of ADC Pd/SnO_2: a-b) High magnification HAADF-STEM images of ADC Pd/SnO_2. Scale bars, 20 nm and 5nm, respectively.

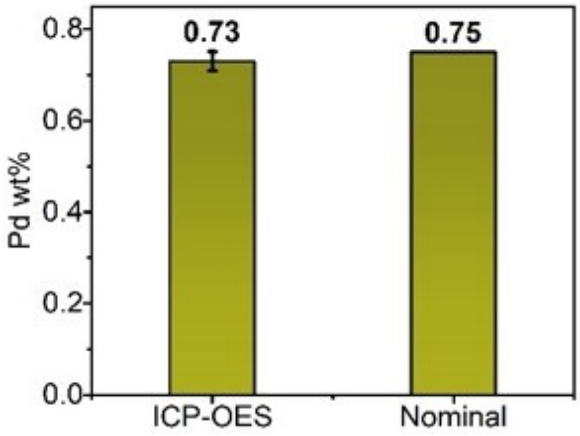

Figure S9. Comparison of actual Pd loading in ADC Pd/SnO_2 quantified via ICP-OES with its nominal loading

Table S1. X-ray photoelectron spectroscopy analyses data

Line (sensitivity factor)	Measured Signal (x 10^3)	Calculated Intensity (x 10^3)
O 1s (0.711)	173	243
Sn $3d_{5/2}$ (4.41)	507	115
Pd 3d (5.00)	90	18

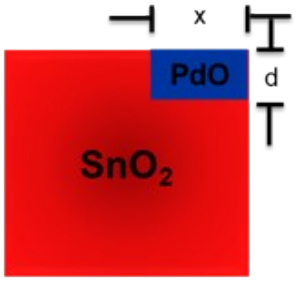

Scheme S2. A simple model assuming one atom thick Pd covers SnO_2 support. x represents the fractional coverage of one-atom thick Pd, d donates 0.3 nm, and λ is Sn photoelectron m.f.p. in Pd = 1.0 nm

The Pd atom number density on SnO_2 was estimated to be:

$$I_{Sn} = I_0[1 - x + xe^{-dI\lambda}] \quad (S1)$$

$$I_{Pd} = I_0 x(1 - e^{-dI\lambda}) \quad (S2)$$

$$\Longrightarrow x \approx 0.53$$

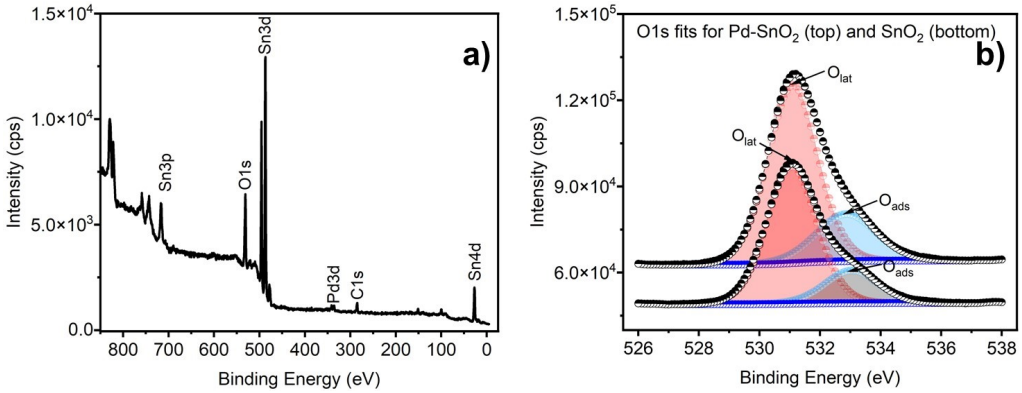

Figure S10. XPS spectra of the as prepared ADC Pd/SnO_2. a) ADC Pd/SnO_2 wide scan. b) Oxygen core level spectra of SnO_2 and ADC Pd/SnO_2: O 1s peaks of SnO_2, and ADC Pd/SnO_2 were deconvoluted and assigned to two major subpeaks. The first peak (O1) at 531.1 eV is attributed to the lattice oxygen vacancies (O_{latt}), the second peak at 532.8 eV to the surface OH group (O_{ads}).

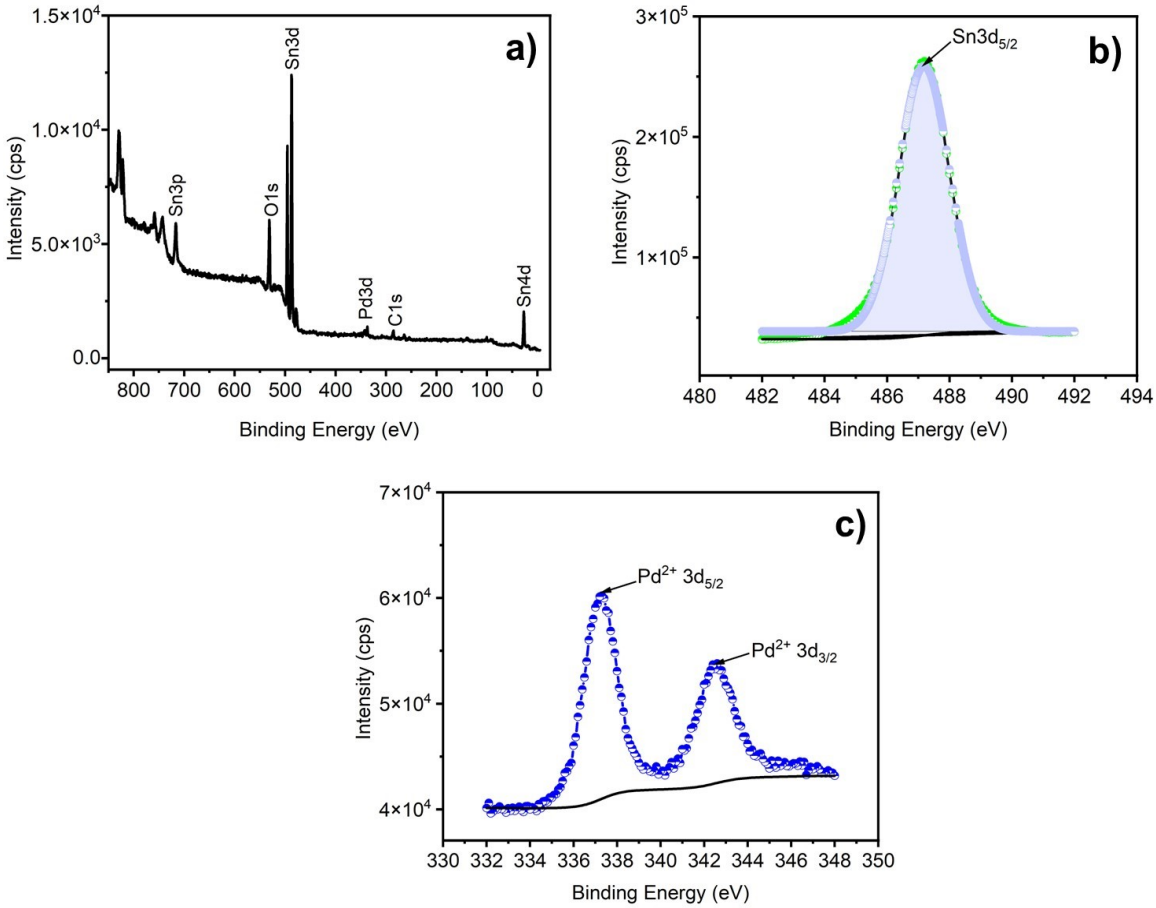

Figure S11. XPS characterization of Pd NP/SnO_2: a) The full spectrum scan of XPS; b) Sn $3d_{5/2}$ region of Pd NP/SnO_2; c) Pd 3d region of Pd NP/SnO_2.

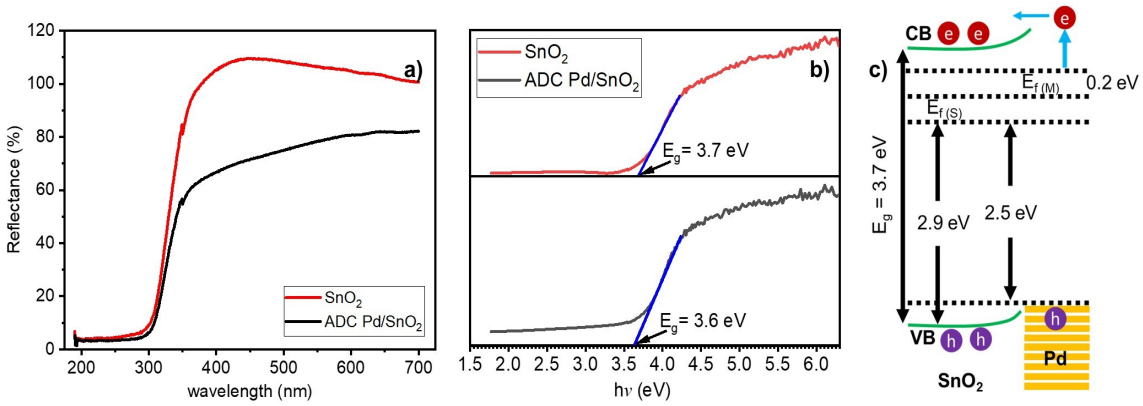

Figure S12. a) UV-vis diffuse reflectance spectra (DRS) of pure SnO_2 and ADC Pd/SnO_2; b) Respective Kubelka Munk function for estimating the band gap energy. c) Proposed band structure diagram for SnO_2 and ADC Pd/SnO_2.

Table S2. Types and number of scattering paths expected for different structural models. The ADC Model 3 is consistent with the EXAFS modeling of ADC Pd/SnO_2 sample.

	Pd-Pd interaction			Pd-Sn interaction		
PdO Sheet	**Scattering Path**	**CN**	**R (Å)**	**Scattering Path**	**CN**	**R (Å)**
	Pd-O	4	2.01	Pd-O	-	-
	Pd-Pd	2	3.02	Pd-Sn	-	-
	Pd-Pd	-	-	Pd-Sn	-	-
ADC Model 1 Pd_2O_6 anchored vertically on O atoms of SnO_2	**Scattering Path**	**CN**	**R (Å)**	**Scattering Path**	**CN**	**R (Å)**
	Pd-O	4	2.01	Pd-O	-	-
	Pd-Pd	1	3.02	Pd-Sn	1	2.21
	Pd-Pd	-	-	Pd-Sn	-	-
ADC Model 2 Pd_2O_6 anchored vertically on Sn atoms of SnO_2	**Scattering Path**	**CN**	**R (Å)**	**Scattering Path**	**CN**	**R (Å)**
	Pd-O	4	2.01	Pd-O	-	-
	Pd-Pd	1	3.02	Pd-Sn	-	-
	Pd-Pd	-	-	Pd-Sn	1	3.90
ADC Model 3 Pd_2O_6 flat on the surface of SnO_2	**Scattering Path**	**CN**	**R (Å)**	**Scattering Path**	**CN**	**R (Å)**
	Pd-O	4	2.01	Pd-O	-	-
	Pd-Pd	1	3.02	Pd-Sn	-	-
	Pd-Pd	-	-	Pd-Sn	1	3.40

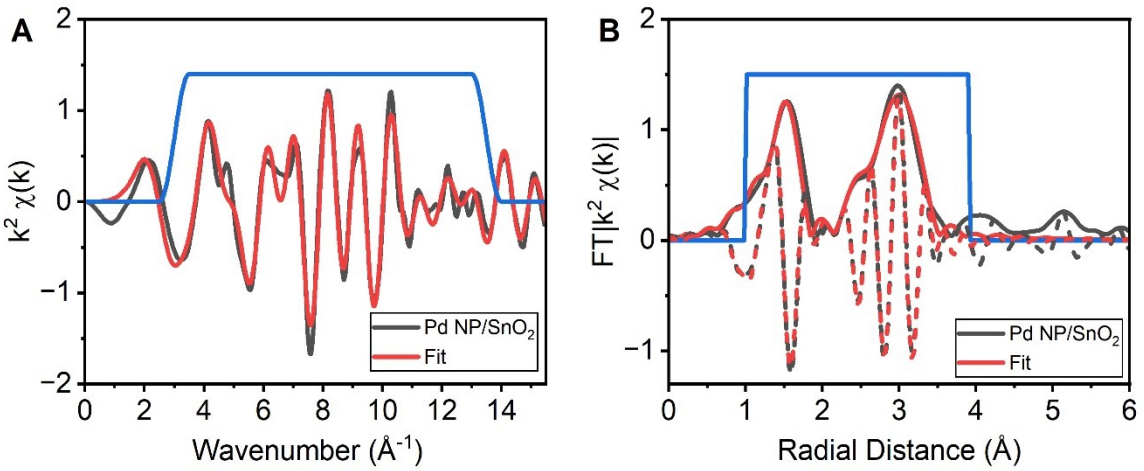

Figure S13. EXAFS modeling of the Pd NPs/SnO_2 using coordination numbers and bond distances of bulk PdO. The detail of the fit is summarized in Table S3. Fitting was performed on the k-range of 3.0 – 13.5 $Å^{-1}$ and R-range of 1.0 – 3.9 Å. S_0^2 was set to 0.78±0.04.

Table S3. Types and number of scattering paths for EXAFS modeling of Pd NP.

Scattering path	**CN**	**R (Å)**	$\sigma^2 \times 10^3 (Å^2)$	ΔE_0 **(eV)**	**R factor (%)**
Pd-O	4	2.01 ± 0.01	1.6 ± 0.7	-5.1 ± 1.3	2.5
Pd-Pd	4	3.04 ± 0.01	4.0 ± 0.6	-5.1 ± 1.3	
Pd-Pd	8	3.43 ± 0.01	4.7 ± 0.5	-5.1 ± 1.3	

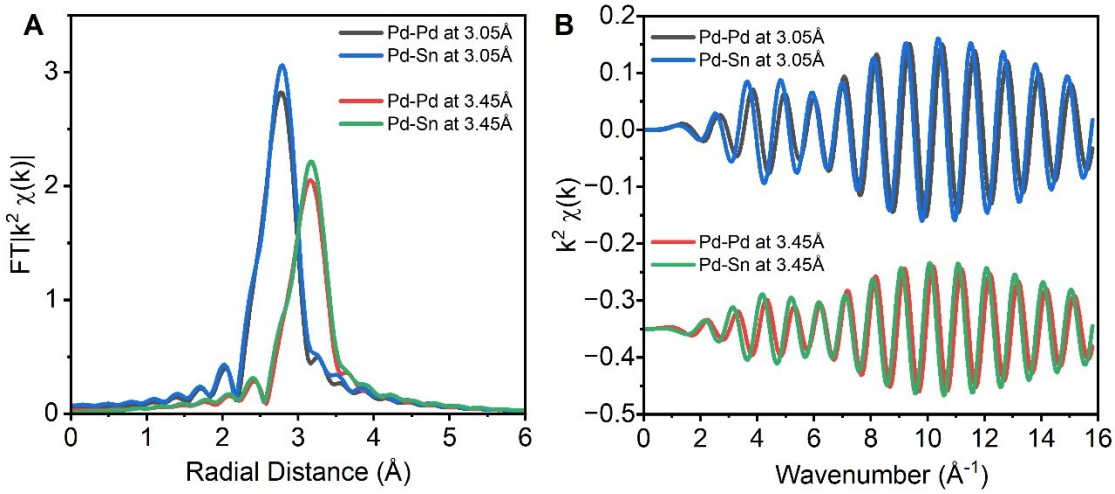

Figure S14. Comparison of Pd-Pd vs. Pd-Sn scattering paths at 3.05 and 3.45 Å in the k^2-weighted (A) magnitude *R*-space and (B) *k*-space.

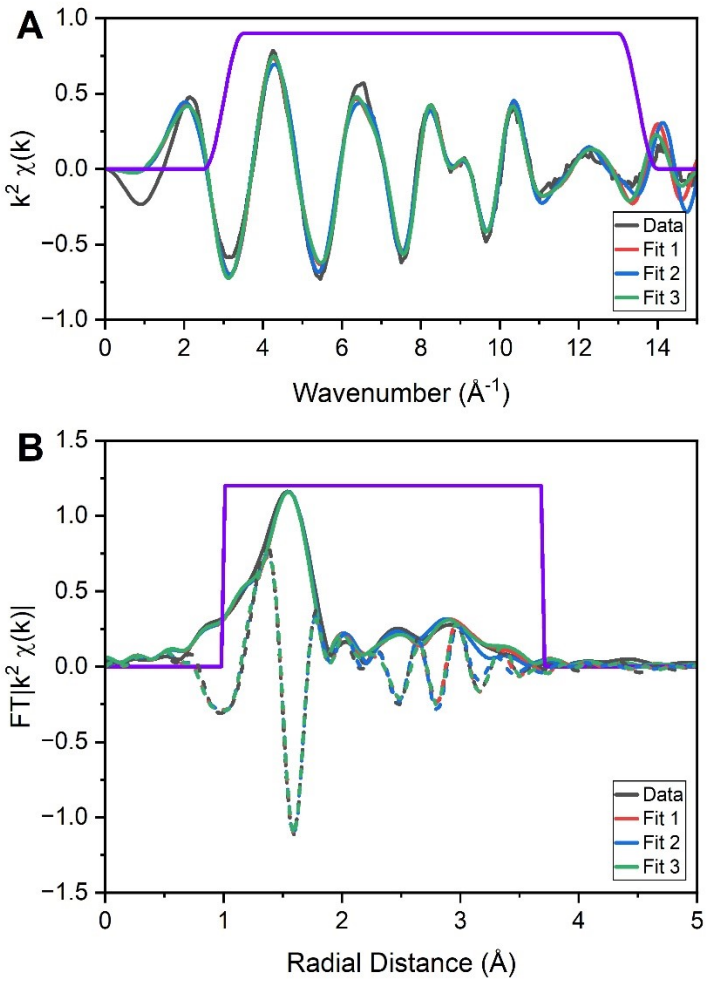

Figure S15. Comparison of the EXAFS modeling of ADC Pd/SnO_2 using different combinations of scattering paths. The data and fits are shown in the k^2-weighted (A) *k*-space and (B) *R*-space in magnitude (solid lines) and imaginary (dotted lines). Fit 1 includes only Pd-Pd paths while fit 2 includes only Pd-Sn paths. Fit 3 includes both Pd-Pd and Pd-Sn. All fits also include Pd-O path. The details of the fits are summarized in Table S4. Fitting was performed on the k-range of 3.0 – 13.5 $Å^{-1}$ and R-range of 1.0 – 3.7 Å.

Table S4. Fitting parameters for the EXAFS of ADC Pd/SnO_2

	Scattering path	**CN**	**R (Å)**	$\sigma^2 \times 10^3 (Å^2)$	ΔE_0 **(eV)**	**R factor (%)**
Fit 1 Pd-Pd only	Pd-O	3.7 ± 0.3	2.02 ± 0.01	1.9 ± 1.0	-2.3 ± 1.3	2.1
	Pd-Pd	0.5 ± 0.5	3.05 ± 0.02	0.2 ± 4.4	-2.3 ± 1.3	
	Pd-Pd	1.3 ± 1.0	3.44 ± 0.02	3.3 ± 4.6	-2.3 ± 1.3	
Fit 2 Pd-Sn only	Pd-O	3.9 ± 0.3	2.02 ± 0.01	2.1 ± 0.8	-3.1 ± 1.2	1.6
	Pd-Sn	0.7 ± 0.5	3.02 ± 0.01	1.7 ± 3.7	-3.1 ± 1.2	
	Pd-Sn	0.9 ± 0.7	3.40 ± 0.02	2.4 ± 4.7	-3.1 ± 1.2	
Fit 3 Pd-Pd & Pd-Sn	Pd-O	3.8 ± 0.3	2.02 ± 0.01	2.0 ± 0.9	-2.4 ± 1.3	1.9
	Pd-Pd	1.0 ± 0.9	3.06 ± 0.02	3.2 ± 4.7	-2.4 ± 1.3	
	Pd-Sn	1.7 ± 1.3	3.44 ± 0.03	6.0 ± 5.5	3.9 ± 3.6	
S_0^2 was set to 0.78±0.04 based on fitting of Pd foil. Fitting was performed on the k-range of 3.0 – 13.5 $Å^{-1}$ and R-range of 1.0 – 3.7 Å. Paths were generated from PdO and Sn-substituted PdO structures.						

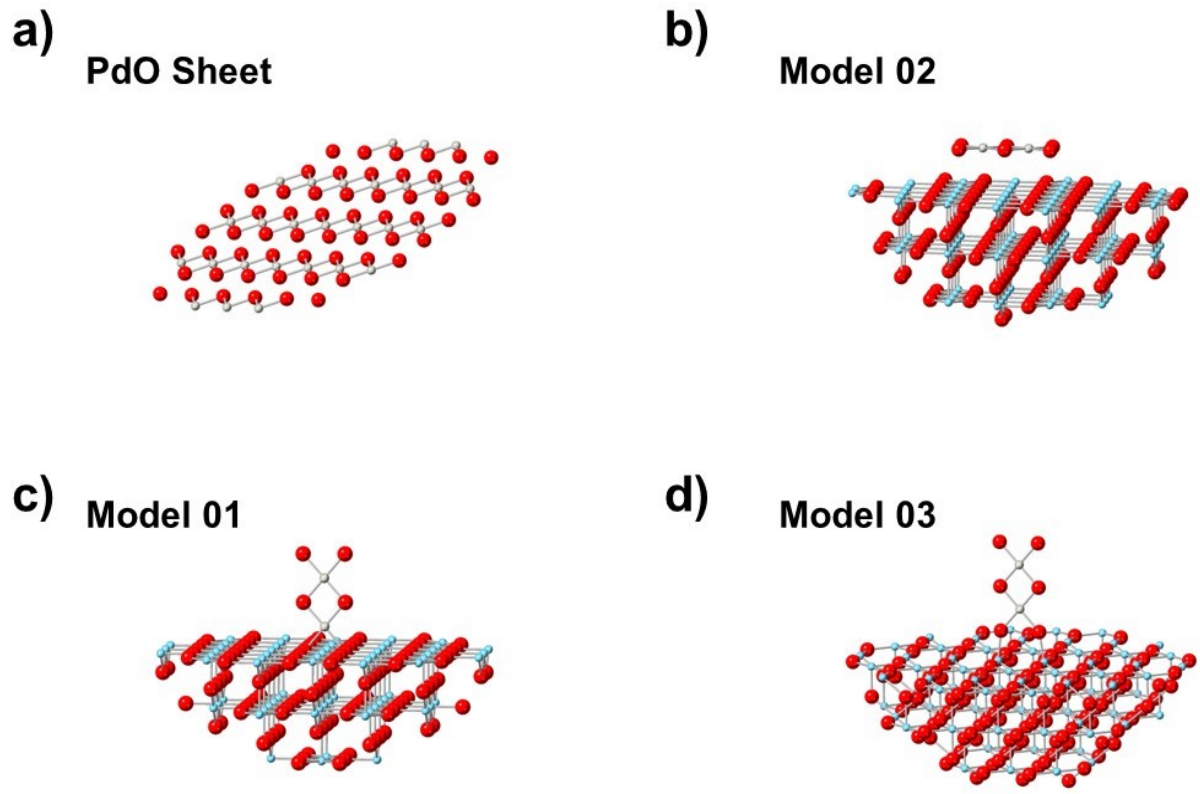

Figure S16. Structural models considered for the ADC Pd/SnO_2. (a) A layer of PdO sheet. (b) Model 1 has a Pd_2O_6 unit anchored vertically on O atoms of SnO_2. (c) Model 2 has a Pd_2O_6 unit anchored vertically on Sn atoms of SnO_2. (d) Model 3 has a Pd_2O_6 lying flat on the surface of SnO_2. (Red: O, Grey: Pd, Blue: Sn)

Table S5. Types and number of scattering paths expected for different structural models. The Model 3 is consistent with the EXAFS modeling of ADC Pd/SnO_2 sample.

	Pd-Pd interaction			**Pd-Sn interaction**		
PdO Sheet	**Scattering Path**	**CN**	**R (Å)**	**Scattering Path**	**CN**	**R (Å)**
	Pd-O	4	2.01	Pd-O	-	-
	Pd-Pd	2	3.02	Pd-Sn	-	-
	Pd-Pd	-	-	Pd-Sn	-	-
Model 1 Pd_2O_6 anchored vertically on O atoms of SnO_2	**Scattering Path**	**CN**	**R (Å)**	**Scattering Path**	**CN**	**R (Å)**
	Pd-O	4	2.01	Pd-O	-	-
	Pd-Pd	1	3.02	Pd-Sn	1	2.21
	Pd-Pd	-	-	Pd-Sn	-	-
Model 2 Pd_2O_6 anchored vertically on Sn atoms of SnO_2	**Scattering Path**	**CN**	**R (Å)**	**Scattering Path**	**CN**	**R (Å)**
	Pd-O	4	2.01	Pd-O	-	-
	Pd-Pd	1	3.02	Pd-Sn	-	-
	Pd-Pd	-	-	Pd-Sn	1	3.90
Model 3 Pd_2O_6 flat on the surface of SnO_2	**Scattering Path**	**CN**	**R (Å)**	**Scattering Path**	**CN**	**R (Å)**
	Pd-O	4	2.01	Pd-O	-	-
	Pd-Pd	1	3.02	Pd-Sn	-	-
	Pd-Pd	-	-	Pd-Sn	1	3.40

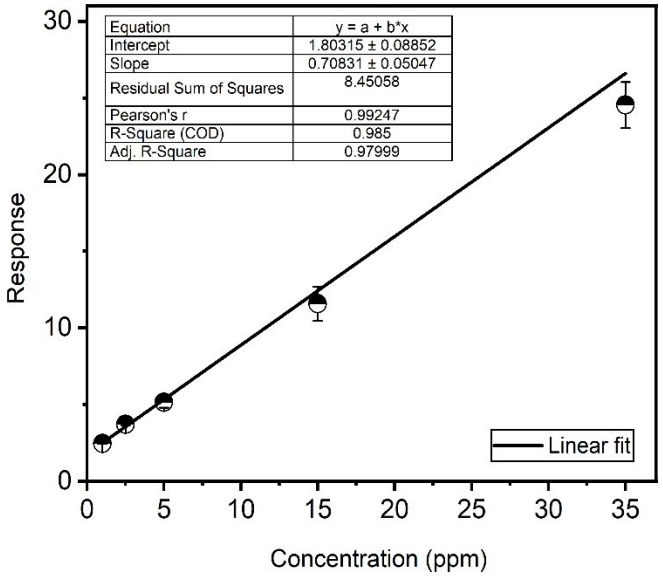

Figure S17. Estimation of limit of detection of the ADC Pd/SnO_2 sensor. Linear fit to the sensor response to CO at varying concentrations between 1-35 ppm at 60 °C.

The LOD of the sensor was calculated by,

$$LOD = \frac{3 \times RMS_{noise}}{slope} \qquad (S3)$$

where RMS_{noise} is the root-mean-square error.

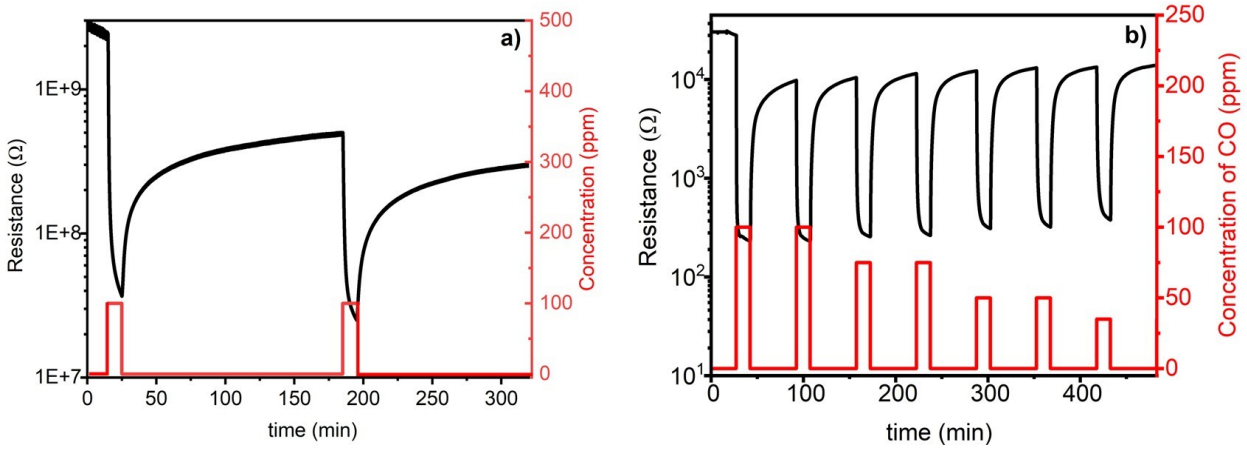

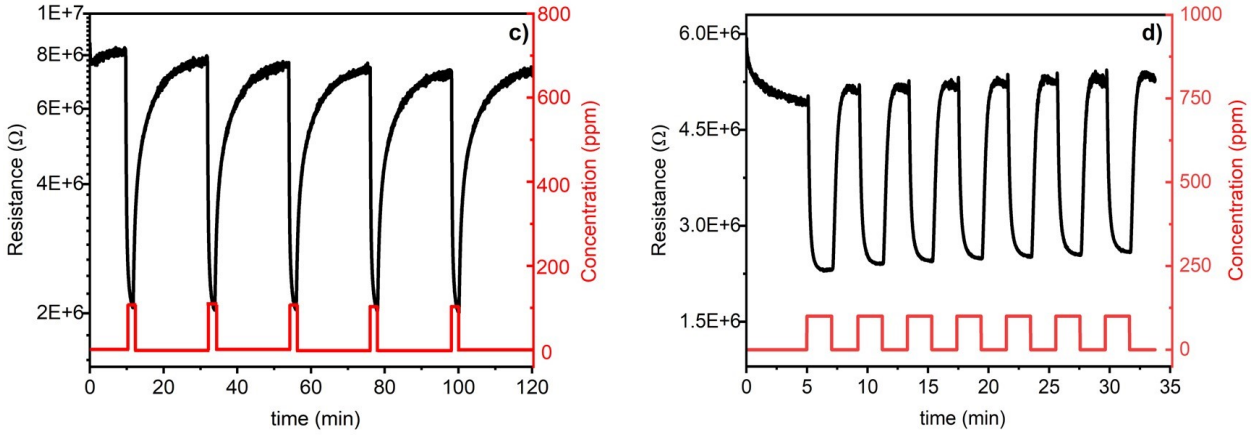

Figure S18. Dynamic response and recovery curves of the ADC Pd/SnO_2 sensor upon exposure to 100 ppm CO at various temperatures between 25-120 °C: a-d) Sensor resistance plots of ADC Pd/SnO_2 to 100 ppm pulses of CO at 25-120 °C.

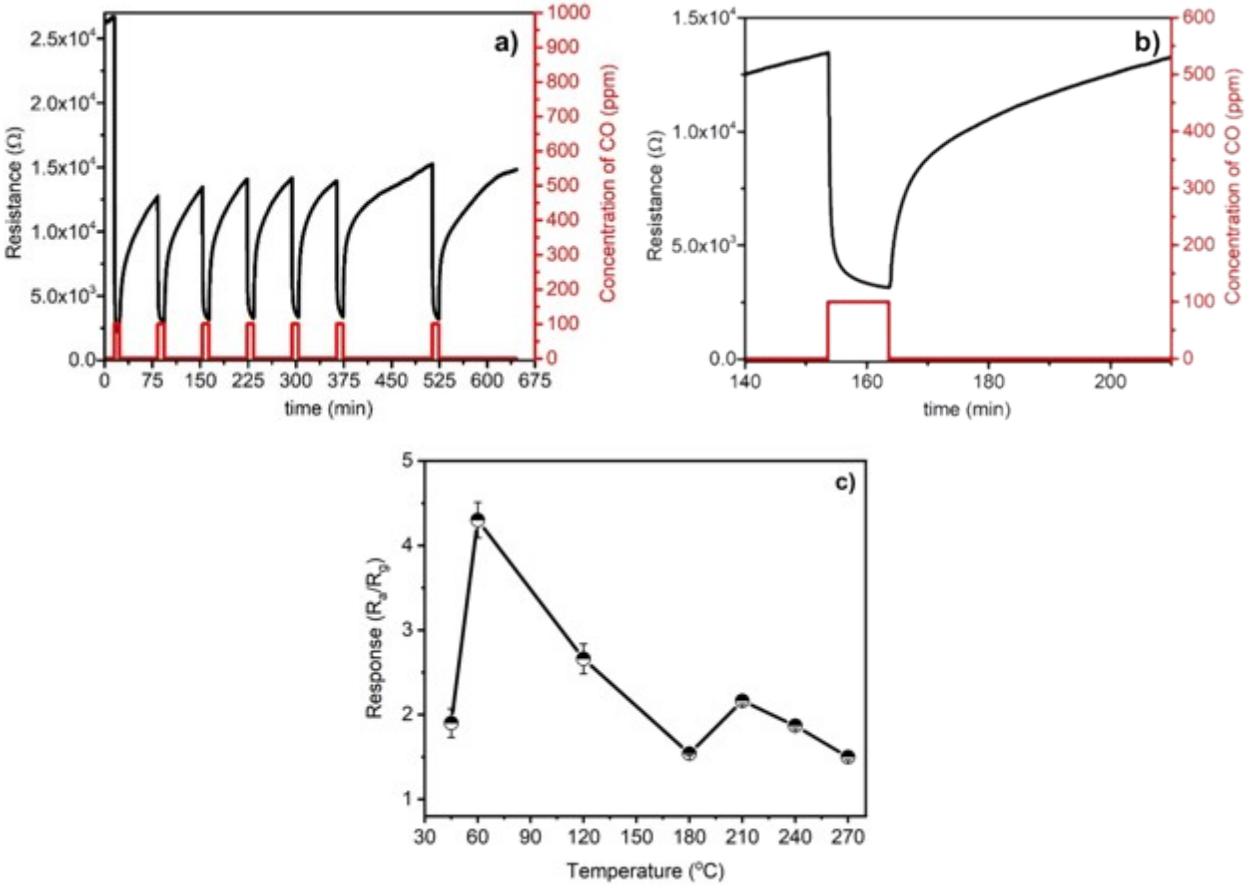

Figure S19. a) Sensor resistance plot of Pd NP/SnO_2 to 100 ppm pulses of CO at 60 °C. b) Extended sensor resistance plot of Pd NP/SnO_2 to 100 ppm pulses of CO at 60 °C during ~ 154-164 min. c) Sensor response to 100 ppm CO at 45-270 °C.

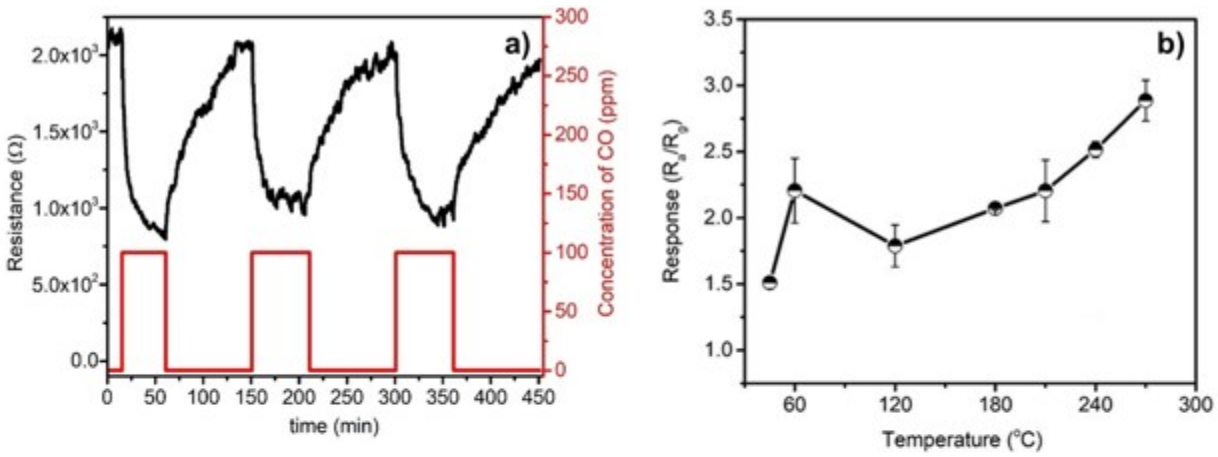

Figure S20. a) Sensor resistance plot of pure SnO_2 to 100 ppm pulses of CO at 60 °C. b) Sensor response to 100 ppm CO at 45-270 °C.

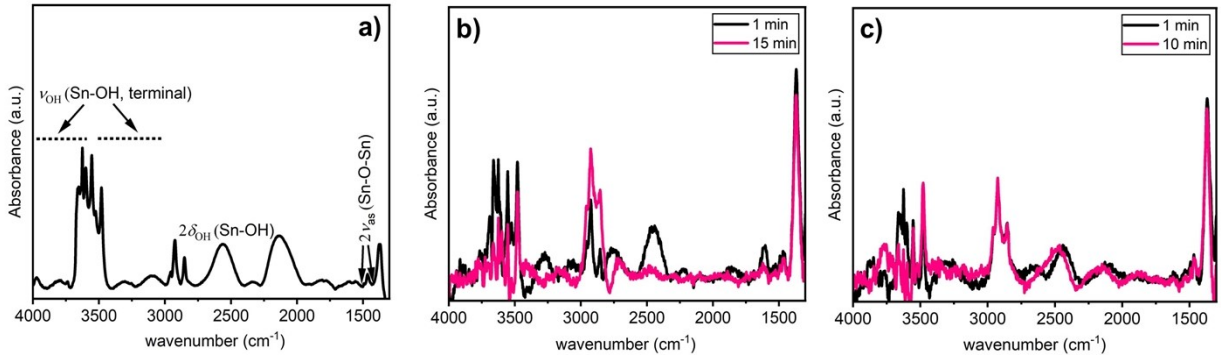

Figure S21. In situ IR spectroscopy of CO interaction with pure SnO_2 in air at 60 °C: a) Prior to CO exposure (4000-1300 cm^{-1}region); b) During dosing of 1000 ppm CO collected at 1 min and 15 min (4000-1300 cm^{-1} region); c) After CO removal acquired at 1 min and 10 min (4000-1300 cm^{-1}region).

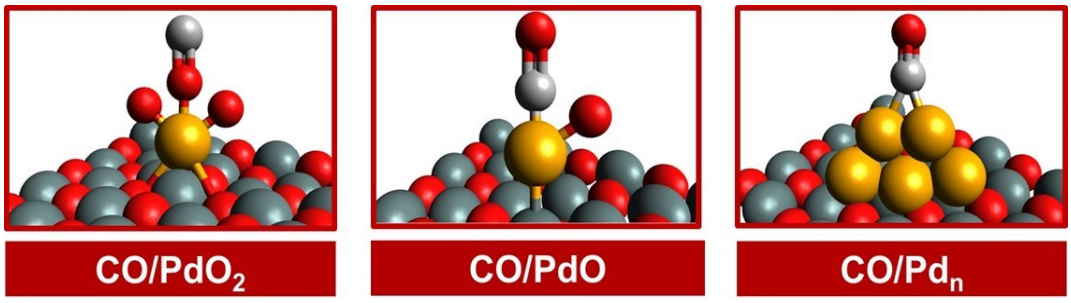

Figure S22. Illustration of the different CO adsorption sites on ADC Pd/SnO_2. Pd, Sn, C, and O atoms are displayed as orange, dark gray, light gray and red spheres, respectively.: CO linearly adsorbed on isolated, positively charged single Pd atoms, CO linearly adsorbed on atop geometry

on Pd single atoms bound to SnO_2 support *via* one oxygen atom, and bridging CO adsorbed on the metallic Pd cluster, respectively.

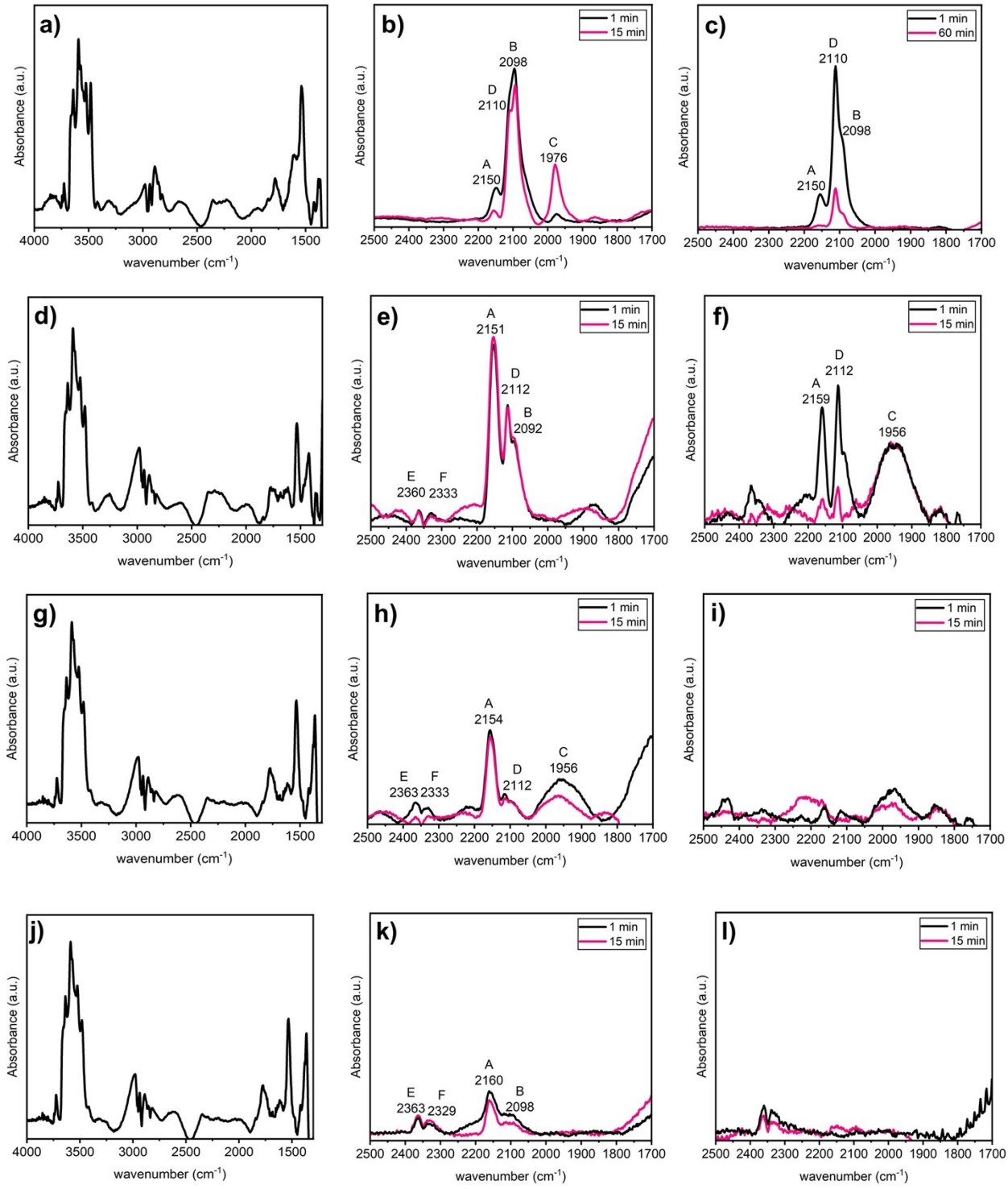

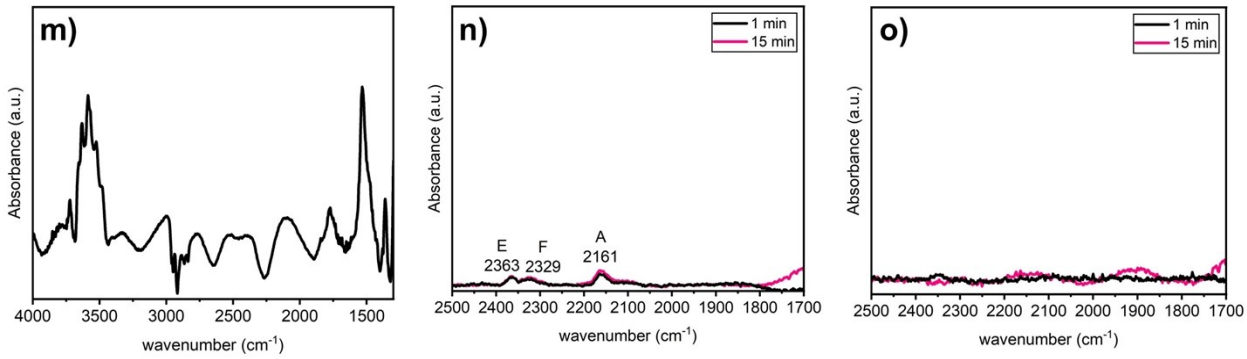

Figure S23. In situ IR spectroscopy of CO interaction with ADC Pd/SnO_2 in air at 120-270 °C a) In situ IR spectra (4000-1300 cm^{-1}) in air at 120 °C and at ambient pressure after calcination at 270 °C b) In situ FTIR spectra (2500–1700 cm^{-1}) during dosing of 1000 ppm CO in air at 120 °C and at ambient pressure collected at various times c) In situ FTIR spectra (2500–1700cm^{-1}) after CO exposure at 120 °C acquired at various times. d) In situ IR spectra (4000-1300 cm^{-1}) in air at 180 °C and at ambient pressure after calcination at 270 °C e) In situ FTIR spectra (2500–1700 cm^{-1}) during dosing of 1000 ppm CO in air at 180 °C and at ambient pressure collected at various times f) In situ FTIR spectra (2500–1700 cm^{-1}) after CO exposure at 180 °C acquired at various times. CO oxidation on ADC Pd/SnO_2 g) In situ IR spectra (4000-1300 cm^{-1}) in air at 210 °C and at ambient pressure after calcination at 270 °C h) In situ FTIR spectra (2500–1700 cm^{-1}) during dosing of 1000 ppm CO in air at 210 °C and at ambient pressure collected at various times i) In situ FTIR spectra (2500–1700 cm^{-1}) after CO exposure at 210 °C acquired at various times. j) In situ IR spectra (4000-1300 cm^{-1}) in air at 240 °C and at ambient pressure after calcination at 270 °C k) In situ FTIR spectra (2500–1700 cm^{-1}) during dosing of 1000 ppm CO in air at 240 °C and at ambient pressure collected at various times l) In situ FTIR spectra (2500–1700 cm^{-1}) after CO exposure at 240 °C acquired at various times. m) In situ IR spectra (4000-1300 cm^{-1}) in air at 270 °C and at ambient pressure after calcination at 270 °C n) In situ FTIR spectra (2500–1700 cm^{-1}) during dosing of 1000 ppm CO in air at 270 °C and at ambient pressure collected at various times o) In situ FTIR spectra (2500–1700 cm^{-1}) after CO exposure at 270 °C acquired at various times.

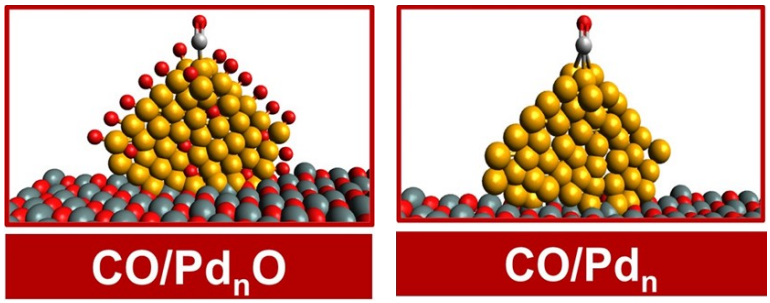

Figure S24. Illustration of the different CO adsorption sites on Pd NP/SnO_2. Pd, Sn, C, and O atoms are displayed as orange, dark gray, light gray and red spheres, respectively.: CO linearly adsorbed on atop PdO nanoclusters and bridging CO adsorbed on metallic Pd NPs, respectively.

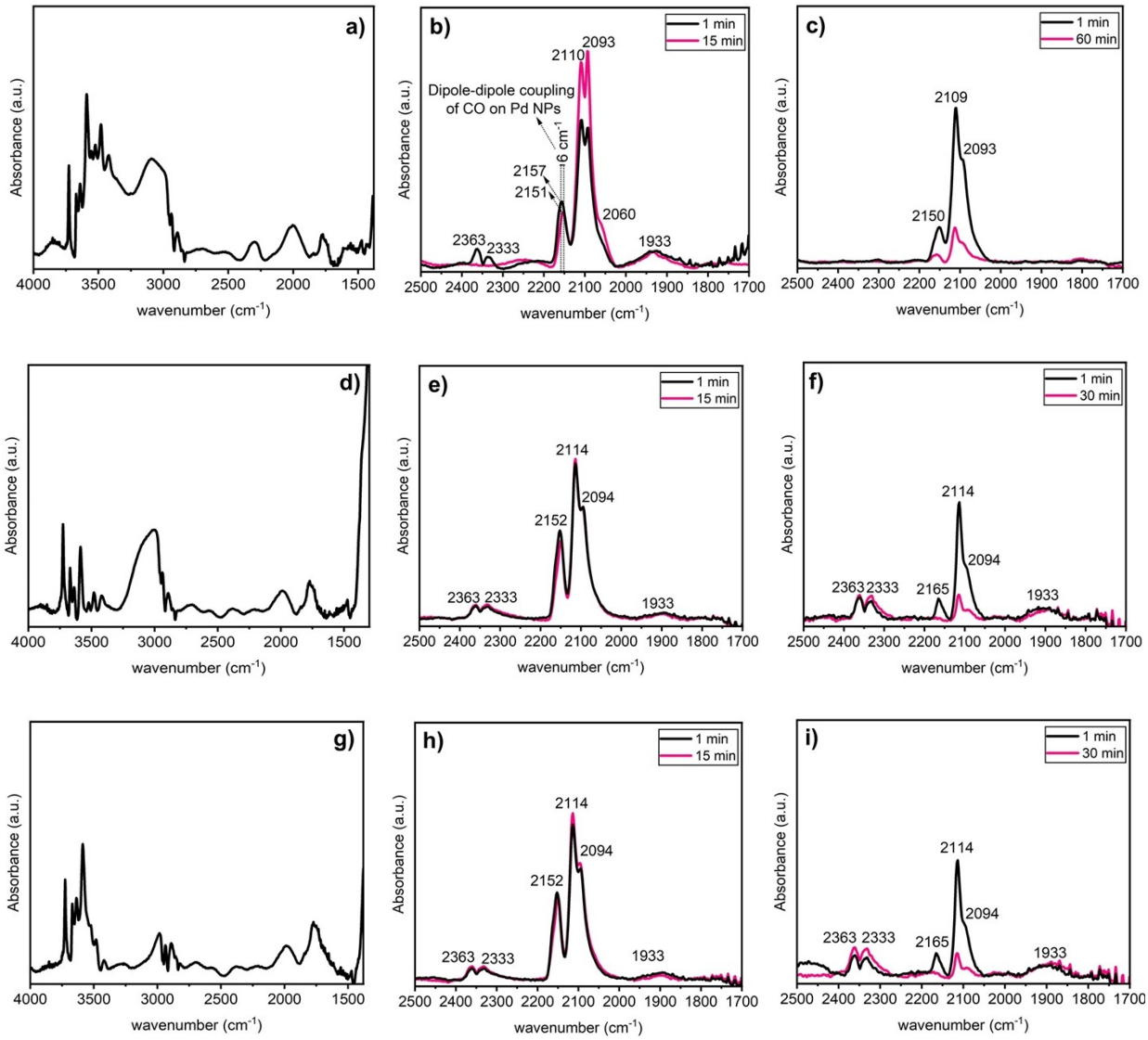

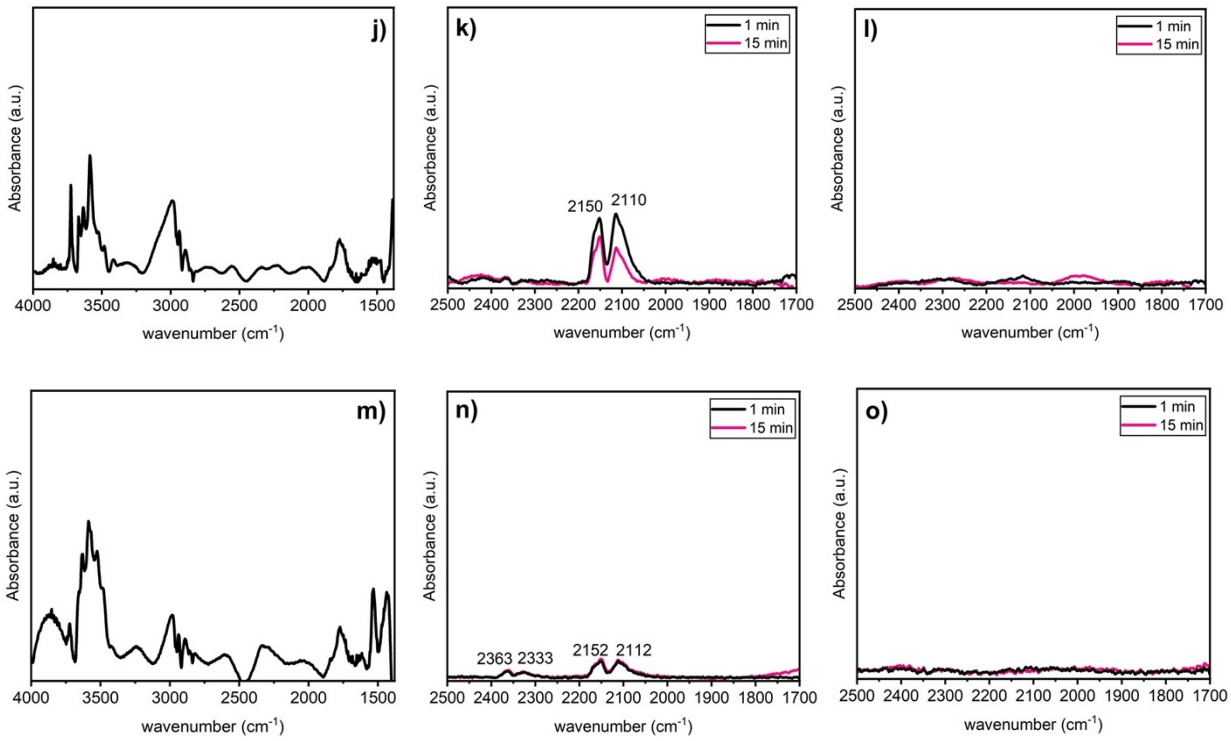

Figure S25. In situ IR spectroscopy of CO interaction with Pd NP/SnO_2 in air at 120-270 °C a) In situ IR spectra (4000-1300 cm^{-1}) in air at 120 °C and at ambient pressure after calcination at 270 °C b) In situ FTIR spectra (2400–1750 cm^{-1}) during dosing of 1000 ppm CO in air at 120 °C and at ambient pressure collected at various times c) In situ FTIR spectra (2350–1850 cm^{-1}) after CO exposure at 120 °C acquired at various times. d) In situ IR spectra (4000-1300 cm^{-1}) in air at 180 °C and at ambient pressure after calcination at 270 °C e) In situ FTIR spectra (2500–1800 cm^{-1}) during dosing of 1000 ppm CO in air at 180 °C and at ambient pressure collected at various times f) In situ FTIR spectra (2450–1800 cm^{-1}) after CO exposure at 180 °C acquired at various times. CO oxidation on ADC Pd/SnO_2 g) In situ IR spectra (4000-1300 cm^{-1}) in air at 210 °C and at ambient pressure after calcination at 270 °C h) In situ FTIR spectra (2500–1800 cm^{-1}) during dosing of 1000 ppm CO in air at 210 °C and at ambient pressure collected at various times i) In situ FTIR spectra (2500–1800 cm^{-1}) after CO exposure at 210 °C acquired at various times. j) In situ IR spectra (4000-1300 cm^{-1}) in air at 240 °C and at ambient pressure after calcination at 270 °C k) In situ FTIR spectra (2500–1800 cm^{-1}) during dosing of 1000 ppm CO in air at 240 °C and at ambient pressure collected at various times l) In situ FTIR spectra (2550–1900 cm^{-1}) after CO exposure at 240 °C acquired at various times. m) In situ IR spectra (4000-1300 cm^{-1}) in air at 270 °C and at ambient pressure after calcination at 270 °C n) In situ FTIR spectra (2500–1800 cm^{-1})

during dosing of 1000 ppm CO in air at 270 °C and at ambient pressure collected at various times o) In situ FTIR spectra (2550–1750 cm^{-1}) after CO exposure at 270 °C acquired at various times.

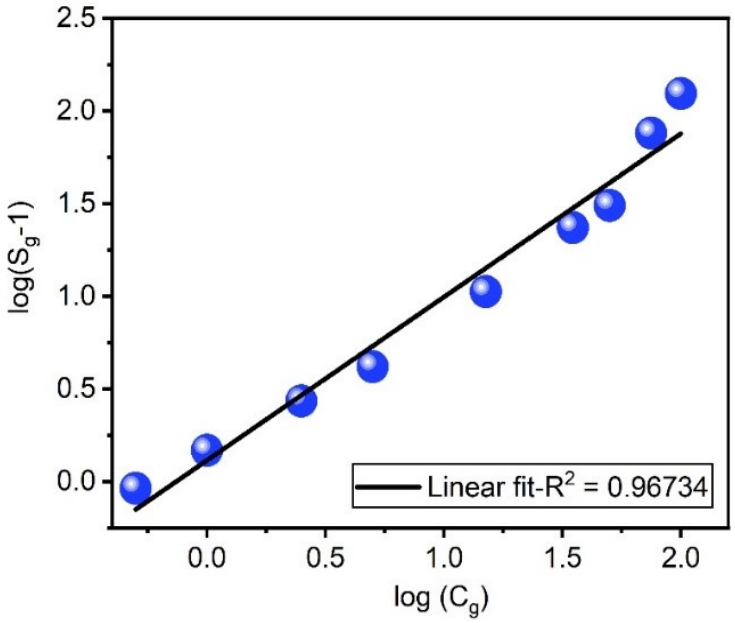

Figure S26. Log (S_g-1) vs. log C_g curve of ADC Pd/SnO_2 sensor response to CO at 60 °C, where S_g is the sensor response (defined previously as R_a/R_g), expressed by Equation 1 in the main text and C_g is the gas concentration.